



# Repeated quantum error detection in a surface code

Christian Kraglund Andersen ✉, Ants Remm , Stefania Lazar, Sebastian Krinner, Nathan Lacroix, Graham J. Norris, Mihai Gabureac, Christopher Eichler and Andreas Wallraff

The realization of quantum error correction is an essential ingredient for reaching the full potential of fault-tolerant universal quantum computation. Using a range of different schemes, logical qubits that are resistant to errors can be redundantly encoded in a set of error-prone physical qubits. One such scalable approach is based on the surface code. Here we experimentally implement its smallest viable instance, capable of repeatedly detecting any single error using seven superconducting qubits—four data qubits and three ancilla qubits. Using high-fidelity ancilla-based stabilizer measurements, we initialize the cardinal states of the encoded logical qubit with an average logical fidelity of 96.1%. We then repeatedly check for errors using the stabilizer readout and observe that the logical quantum state is preserved with a lifetime and a coherence time longer than those of any of the constituent qubits when no errors are detected. Our demonstration of error detection with its resulting enhancement of the conditioned logical qubit coherence times is an important step, indicating a promising route towards the realization of quantum error correction in the surface code.

The feasibility of quantum simulations and computations with more than 50 qubits has been demonstrated in recent experiments<sup>1–3</sup>. Many near-term efforts in quantum computing are currently focused on the implementation of applications for noisy intermediate-scale quantum devices<sup>4</sup>. However, to harness the full potential of quantum computers, fault-tolerant quantum computing must be implemented. Quantum error correction and fault tolerance have been explored experimentally in a variety of physical platforms such as NMR<sup>5</sup>, trapped ions<sup>6–9</sup>, photonics<sup>10,11</sup>, NV centres<sup>12</sup> and superconducting circuits<sup>13–18</sup>. In particular, recent experiments have demonstrated quantum-state stabilization<sup>19–22</sup>, simple error correction codes<sup>7,15,16,23,24</sup> and the fault-tolerant encoding of logical quantum states<sup>9,25</sup>. Quantum error correction with logical error rates comparable to or below those of the physical constituents has also been achieved by encoding quantum information in continuous variables using superconducting circuits<sup>18,26,27</sup>. These bosonic encoding schemes take advantage of high-quality-factor microwave cavities, which are predominantly limited by photon loss. However, so far no repeated detection of both amplitude and phase errors on an encoded logical qubit has been realized in any qubit architecture. In this work, we present such a demonstration using the surface code<sup>28–31</sup>, which, due to its high error threshold, is one of the most promising architectures for large-scale fault-tolerant quantum computing.

In stabilizer codes for quantum error correction<sup>32,33</sup>, a set of commuting multiqubit operators is repeatedly measured, which projects the qubits onto a degenerate eigenspace of the stabilizers referred to as the code space. Thus, the experimental realization of quantum error detection crucially relies on high-fidelity entangling gates between the data qubits and the ancilla qubits and on the simultaneous high-fidelity single-shot readout of all ancilla qubits. For superconducting circuits, multiplexed readout has recently been implemented for high-fidelity simultaneous readout in multiqubit architectures<sup>34–36</sup> with small crosstalk<sup>37</sup>. Small readout crosstalk leading to minimal unwanted dephasing of data qubits when performing ancilla readout has been a key enabler of recent experiments in superconducting circuits realizing repeated ancilla-based

parity detection<sup>21,22</sup>. Moreover, repeatable high-fidelity single- and two-qubit gates<sup>38,39</sup>, required for quantum error correction, have also been demonstrated for superconducting qubits. Here, we utilize low-crosstalk multiplexed readout and a sequential stabilizer measurement scheme<sup>40</sup> for implementing a surface code with seven superconducting qubits.

In the surface code, as in any stabilizer code, errors are detected by observing changes in the stabilizer measurement outcomes. Such syndromes are typically measured by entangling the stabilizer operators with the state of ancilla qubits, which are then projectively measured to yield the stabilizer outcomes. The surface code consists of a  $d \times d$  grid of data qubits with  $d^2 - 1$  ancilla qubits, each connected to up to four data qubits<sup>31</sup>. The code can detect  $d - 1$  errors and correct up to  $\lfloor (d - 1)/2 \rfloor$  errors per cycle of stabilizer measurements. In particular, the stabilizers of the  $d = 2$  surface code (Fig. 1) are given by

$$X_{D1}X_{D2}X_{D3}X_{D4} \quad Z_{D1}Z_{D3} \quad Z_{D2}Z_{D4} \quad (1)$$

For the code distance  $d = 2$ , it is only possible to detect a single error per round of stabilizer measurements, and once an error is detected the error cannot be unambiguously identified; for example, we would obtain the same syndrome outcome for an  $X$  error on D1 and on D3.

Here we use the following logical qubit operators:

$$Z_L = Z_{D1}Z_{D2} \quad \text{or} \quad Z_L = Z_{D3}Z_{D4} \quad (2)$$

$$X_L = X_{D1}X_{D3} \quad \text{or} \quad X_L = X_{D2}X_{D4} \quad (3)$$

such that the code space in terms of the physical qubit states is spanned by the logical qubit states

$$|0\rangle_L = \frac{1}{\sqrt{2}}(|0000\rangle + |1111\rangle) \quad (4)$$

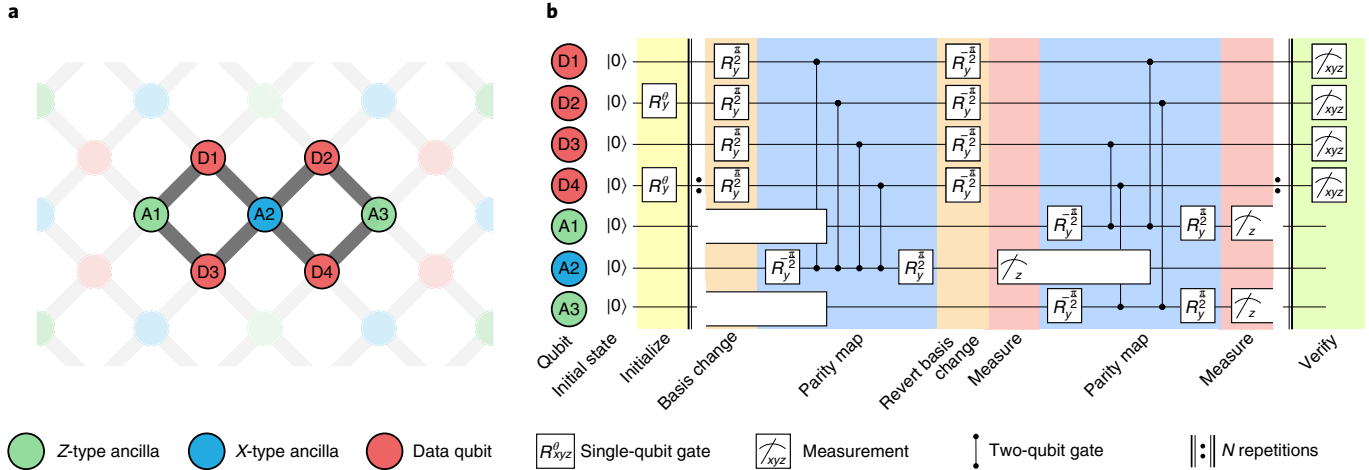


**Fig. 1 | Surface code implemented with seven qubits.** **a**, The surface code consists of a two-dimensional array of qubits. Here the data qubits are shown in red and the ancilla qubits for measuring X-type (Z-type) stabilizers in blue (green). The smallest surface code consists of seven qubits indicated by D1–D4 and A1–A3. **b**, The gate sequence for quantum error detection using the surface code with seven physical qubits. Details of the gate sequence are discussed in the text.

$$|1\rangle_L = \frac{1}{\sqrt{2}}(|0101\rangle + |1010\rangle) \quad (5)$$

To encode quantum information in the logical subspace, we initialize the data qubits in a separable state, chosen such that after a single cycle of stabilizer measurements, and conditioned on ancilla measurement outcomes being  $|0\rangle$ , the data qubits are encoded into the target logical qubit state. In this work, we demonstrate this probabilistic preparation scheme for the logical states  $|0\rangle_L$ ,  $|1\rangle_L$ ,  $|+\rangle_L = (|0\rangle_L + |1\rangle_L)/\sqrt{2}$  and  $|-\rangle_L = (|0\rangle_L - |1\rangle_L)/\sqrt{2}$ , and we perform repeated error detection on these states.

### Implementation of the surface code

The distance-2 surface code, as discussed above, can be realized with a set of seven qubits laid out as depicted in Fig. 1a. The logical qubit is encoded into four data qubits (D1–D4), and three ancilla qubits (A1–A3) are used to measure the three stabilizers  $Z_{D1}Z_{D3}$ ,  $X_{D1}X_{D2}X_{D3}X_{D4}$  and  $Z_{D2}Z_{D4}$ , respectively. We initially herald all qubits in the  $|0\rangle$  state<sup>41,42</sup> and subsequently prepare the data qubits in a product state using single-qubit rotations around the  $y$  axis. These initial states are then projected onto the code space after the initial stabilizer measurement cycle.

We perform the  $X_{D1}X_{D2}X_{D3}X_{D4}$  stabilizer measurement by first applying basis change pulses ( $R_y^{\pi/2}$ ) on the data qubits to map the  $X$  basis to the  $Z$  basis. Then we perform the entangling gates as in Fig. 1b and finally we revert the basis change. The measurement of A2 will therefore yield the  $|0\rangle$  state ( $|1\rangle$  state) corresponding to the eigenvalue  $+1$  ( $-1$ ) of the stabilizer  $X_{D1}X_{D2}X_{D3}X_{D4}$ . While the measurement pulse for A2 is still being applied, we perform the  $Z_{D1}Z_{D3}$  and  $Z_{D2}Z_{D4}$  stabilizer measurements simultaneously using the ancilla qubits A1 and A3, respectively. To avoid unwanted interactions during entangling gate operations, we operate the surface code using a pipelined approach similar to the scheme introduced by Versluis et al.<sup>40</sup>, for which we perform  $X$ -type and  $Z$ -type stabilizer measurements sequentially (Fig. 1b and Supplementary Information). The cycle is repeated after this step, and after  $N$  stabilizer measurement cycles we perform state tomography of the data qubits.

The gate sequence described above is implemented on the seven-qubit superconducting quantum device shown in Fig. 2a; see Methods for fabrication details and Supplementary Information for device parameters. Each qubit (yellow) is a single-island transmon

qubit<sup>43</sup> and features an individual flux line (green) for frequency tuning and an individual charge line (pink) for single-qubit gates. Additionally, each qubit is coupled to a readout resonator (red) combined with an individual Purcell filter (blue). The Purcell filters protect against qubit decay into the readout circuit<sup>44</sup> and suppress readout crosstalk such that multiplexed ancilla measurements can be performed without detrimental effects on the data qubits<sup>37</sup>. Each Purcell filter is coupled to a feedline, and we perform all measurements by probing each feedline with a frequency-multiplexed readout pulse<sup>37</sup>; see Supplementary Information for a complete characterization of the readout. The qubits are coupled to each other via 1.5-mm-long coplanar waveguide segments (cyan) as displayed in Fig. 1a. The surface code, when implemented with seven physical qubits, requires the central ancilla qubit to connect to four neighbours. The qubit island shape, shown in Fig. 2b, is designed to facilitate coupling to a readout resonator and four two-qubit couplers. To ensure a closed ground plane around the qubit island, each coupler element crosses the ground plane with an airbridge (white). We install the device in a cryogenic measurement set-up<sup>45</sup> (Methods and Extended Data Fig. 1), and we characterize and benchmark the device using time-domain and randomized benchmarking methods as detailed in Supplementary Information.

### Quantum error detection

Changes in the outcome of repeated stabilizer measurements, also referred to as syndromes, signal the occurrence of an error. It is thus critical to directly verify the ability to measure the multiqubit stabilizers using the ancilla readout<sup>46</sup>. We characterize the performance of the ancilla-based stabilizer checks by explicitly measuring the weight-4 stabilizer as well as the two weight-2 stabilizers. For this purpose, we initialize the data qubits in each of the computational basis states and map their parity onto the corresponding ancilla qubit. As the natural measurement basis for the dispersive readout of superconducting qubits is the  $Z$  basis, we perform this characterization measurement in the  $Z$  basis for all three stabilizers, without adding the basis change pulses to turn the  $Z$ -parity measurement into an  $X$ -parity measurement. For the implementation of the full surface code sequence depicted in Fig. 1b, we apply the necessary basis rotation gates on all four data qubits to perform the weight-4 stabilizer check in the  $X$  basis, and then return to the  $Z$  basis by reversing the basis change. For each stabilizer, the other

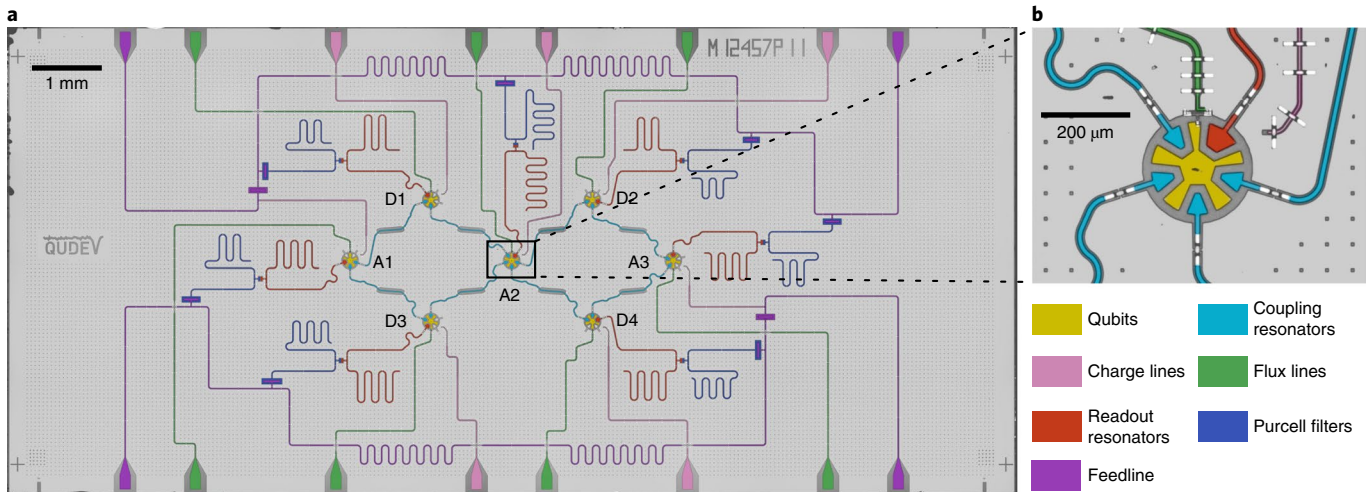


**Fig. 2 | Seven-qubit device.** **a**, False-coloured micrograph of the seven-qubit device used in this work. Transmon qubits are shown in yellow, coupling resonators in cyan, flux lines for single-qubit tuning and two-qubit gates in green, charge lines for single-qubit drive in pink, the two feedlines for readout in purple, transmission line resonators for readout in red and Purcell filters for each qubit in blue. **b**, Enlarged view of the centre qubit (A2), which connects to four neighbouring qubits.

ancilla qubits and unused data qubits are left in the ground state. We correctly assign the ancilla measurement outcome corresponding to the prepared basis state with success probabilities of 95.0%, 83.5% and 91.8% for the stabilizers  $Z_{D_1}Z_{D_3}$ ,  $Z_{D_1}Z_{D_2}Z_{D_3}Z_{D_4}$  and  $Z_{D_2}Z_{D_4}$  calculated as the overlap between the measured probabilities and the ideal case (grey wireframe in Fig. 3). Master-equation simulations, which include decoherence and readout errors, are shown by the red wireframes in Fig. 3. The parity measurements are mainly limited by the relaxation of the data qubits, which directly leads to worse results for states with multiple excitations such as the  $|1111\rangle$  state when measuring  $Z_{D_1}Z_{D_2}Z_{D_3}Z_{D_4}$ . Further variations in the correct parity assignment probability arise due to the differences in qubit lifetimes and two-qubit gate durations (Supplementary Information).

In a next step, we prepare logical states by projecting the data qubits onto the desired code space. We use a probabilistic encoding scheme in which we initialize the data qubits in a given product state and perform one cycle of stabilizer measurements, that is, we perform the gate sequence as depicted in Fig. 1b for  $N=1$ . For those events yielding a measurement result of  $|0\rangle$  for all three syndromes, this scheme projects the data qubits onto the desired logical state. We can use this probabilistic scheme to prepare any logical state by initializing the state  $|0\rangle(a|0\rangle+b|1\rangle)|0\rangle(a|0\rangle+b e^{i\phi}|1\rangle)$ , which will be projected onto the (unnormalized) logical state  $|\psi\rangle_L=a^2|0\rangle_L+b^2 e^{i\phi}|1\rangle_L$ . Here, we specifically initialize the logical states  $|0\rangle_L$ ,  $|1\rangle_L$ ,  $|+\rangle_L$  and  $|-\rangle_L$  by performing one cycle of stabilizer measurements on the states  $|0000\rangle$ ,  $|0101\rangle$ ,  $|0+0+\rangle$  and  $|0+0-\rangle$ , respectively, with  $|\pm\rangle=(|0\rangle\pm|1\rangle)/\sqrt{2}$ .

First, we consider the preparation of  $|0\rangle_L$  for which the data qubit state  $|0000\rangle$  after one cycle of stabilizer measurements is projected onto the state  $|\psi_0\rangle=(|0000\rangle+|1111\rangle)/\sqrt{2}$  when all ancilla qubits are measured in  $|0\rangle$ . We measure all ancilla qubits to be in the  $|0\rangle$  state with a success probability of 25.1%, compared with an expected probability of 50% in the ideal case. To verify the state preparation, we perform full state tomography of the four data qubits after the completion of one cycle of stabilizer measurements and construct the density matrix on the basis of a maximum-likelihood estimation taking readout errors into account. The measured density matrix of the physical data qubits has a fidelity of  $F_{\text{phys}}=\langle\psi_0|\rho|\psi_0\rangle=70.3\%$  to the target state (Fig. 4a,b). While the infidelity is dominated by qubit decoherence, we also observe small residual coherent phase errors as seen by the finite imaginary matrix elements in Fig. 4b,

corresponding to a phase error of  $5^\circ$  accumulated over the cycle time of  $1.92\mu\text{s}$  or, equivalently, a frequency drift of  $7\text{kHz}$  for any qubit.

Given access to the full density matrix, we can project it onto the logical qubit subspace  $\rho_{L,i}=\langle j|\rho|i\rangle/P_L$  for  $|i\rangle$ ,  $|j\rangle\in\{|0\rangle_L, |1\rangle_L\}$ . Here,  $P_L=\sum_i\langle i|\rho|i\rangle$  is the probability for the prepared state to be within the logical subspace, which is also referred to as the acceptance probability<sup>25</sup> or yield<sup>9</sup>. The state  $\rho_L$  is the logical qubit state, conditioned on the prepared state residing in the code space at the end of the cycle. In general,  $F_{\text{phys}}=F_L P_L$ , where  $F_L$  is the fidelity of  $\rho_L$  compared with the ideal logical state. We experimentally find  $P_L=0.717$ . From simulations, we understand that the reduced  $P_L$  mainly arises from decoherence during the stabilizer measurement cycle. After the projection onto the code space, the logical qubit state  $|0\rangle_L$  is described by a single-qubit density matrix (Fig. 4c), which has a fidelity of 98.2% to the ideal logical state. Similarly, we prepare the logical states  $|+\rangle_L$ ,  $|-\rangle_L$  and  $|1\rangle_L$ , shown in Fig. 4d-f, with logical state fidelities of 94.2%, 94.8% and 97.3%, respectively. The corresponding logical fidelities of the four logical states from master-equation simulations are 98.5%, 96.6%, 96.4% and 98.1% (Methods). The slightly lower fidelities for the  $|+\rangle_L$  and  $|-\rangle_L$  states

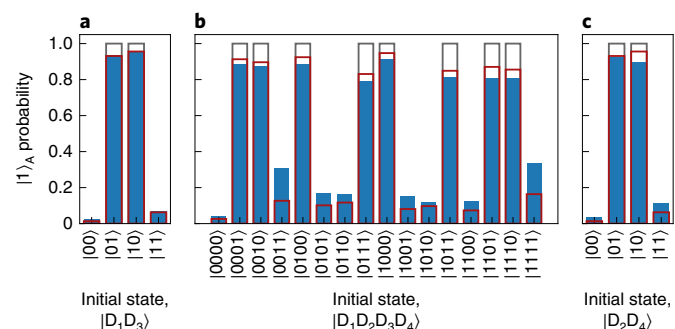


**Fig. 3 | Stabilizer measurements of the data qubits.** **a-c**, The outcomes of the measurement of  $Z_{D_1}Z_{D_3}$  using ancilla  $A=A_1$  (**a**), of  $Z_{D_1}Z_{D_2}Z_{D_3}Z_{D_4}$  using ancilla  $A=A_2$  (**b**) and of  $Z_{D_2}Z_{D_4}$  using ancilla  $A=A_3$  (**c**). For all panels, we show the ideal outcome in the grey wireframe and the corresponding master-equation simulations in the red wireframe.

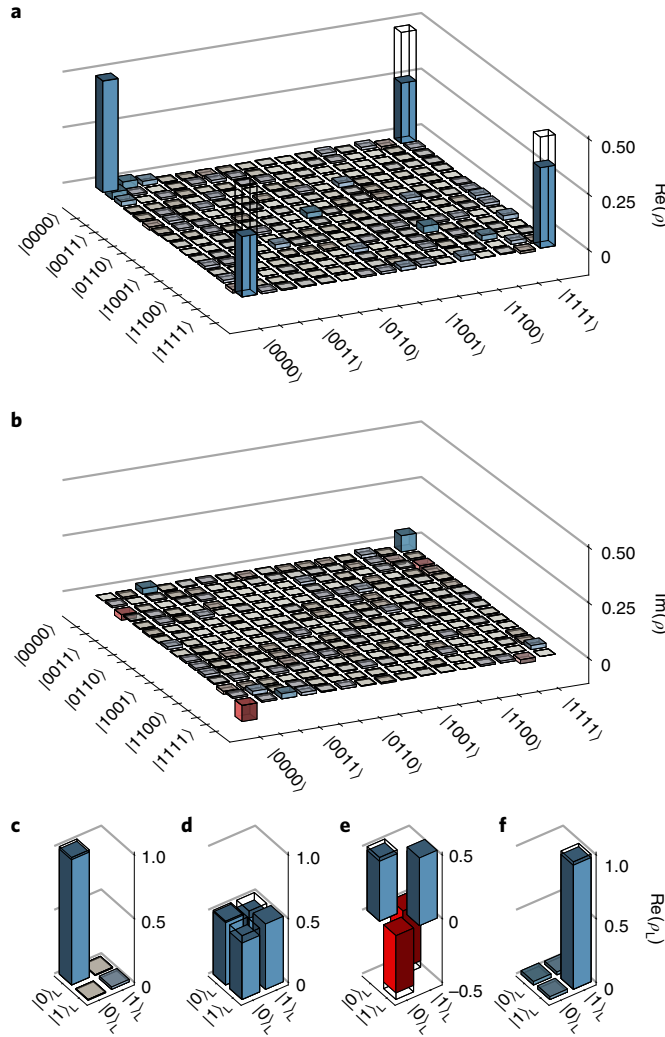


**Fig. 4 | Preparation of logical states.** **a,b,** Real (**a**) and imaginary (**b**) parts of the density matrix of the four physical data qubits prepared in the  $|0\rangle_L$  state using a single round of stabilizer measurements. The fidelity to the target state, shown in the wireframe, is 70.3%. **c,** Real part of  $\rho_L$ , that is the density matrix shown in **a** and **b**, projected onto the logical subspace. The fidelity to the target logical state is 98.2%. **d-f,** Density matrices for the logical states  $|+\rangle_L$  (**d**),  $|- \rangle_L$  (**e**) and  $|1\rangle_L$  (**f**). The corresponding logical fidelities are 94.2%, 94.8% and 97.3%, respectively.

arise from the pure dephasing of the data qubits, making  $Z$  errors during the encoding more likely than  $X$  errors.

Next, we demonstrate repeated quantum error detection of any single error, which is a key ingredient of quantum error correction schemes such as the surface code. We characterize the performance of the error detection scheme by measuring the expectation value of the encoded qubit's logical  $Z_L$  ( $X_L$ ) operator conditioned on having detected no error in any repetition of the stabilizer measurement and on having the final measurement of the data qubits satisfy  $Z_{D1}Z_{D3}=Z_{D2}Z_{D4}=1$  ( $X_{D1}X_{D2}X_{D3}X_{D4}=1$ ). This latter condition ensures that the qubits have remained in the logical subspace during the last detection cycle. We find that the expectation value  $\langle Z_L \rangle$  (green and blue data points) decays in good approximation exponentially from unity with a logical lifetime of  $62.7 \pm 9.4 \mu\text{s}$  from this exponential fit, which exceeds the lifetime,  $16.8 \mu\text{s}$ , of the best physical qubit (dashed lines) of the device (Fig. 5a). The logical expectation values

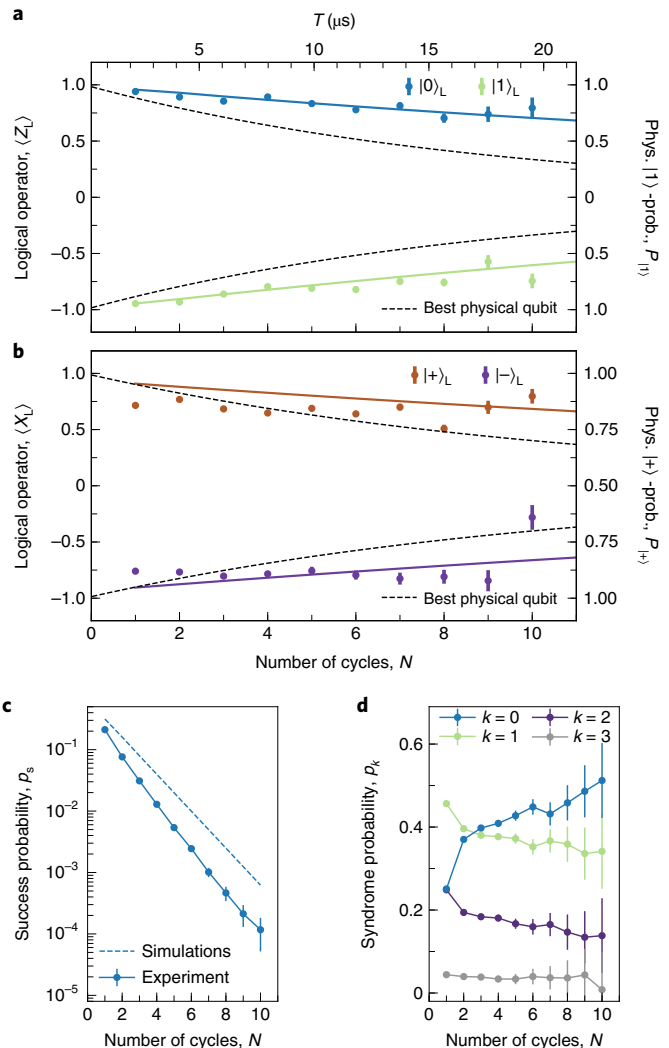


**Fig. 5 | Repeated quantum error detection.** **a,b,** The expectation values of the logical  $Z_L$  operator (**a**) and the logical  $X_L$  operator (**b**) as a function of  $N$ . The expectation values are shown for the prepared  $|0\rangle_L$ ,  $|1\rangle_L$ ,  $|+\rangle_L$  and  $|-\rangle_L$  states. The solid lines indicate the corresponding values obtained from master-equation simulations. Also shown (dashed lines, right axis) are the qubit decay of the  $|1\rangle$  state with the best measured  $T_1$  value (**a**) and the physical qubit decoherence of the  $|+\rangle$  state with the best measured  $T_2$  value (**b**). **c,** Total success probability  $p_s$  for detecting no errors during  $N$  cycles of stabilizer measurements for the  $|0\rangle_L$  data shown in **a** and the corresponding values from numerical simulations. **d,** Probability of observing  $k$  ancilla qubits in the  $|1\rangle$  state for each measurement cycle conditioned on having detected no error in any of the previous  $N-1$  cycles. The data correspond to the initial  $|0\rangle_L$  state presented in **a**. The error bars in all panels represent s.d.

are evaluated after the  $N$ th cycle at time  $T=(1.92N+0.3)\mu\text{s}$  shown on the top axis of Fig. 5a,b. The approximately exponential decay of the logical qubit expectation value  $\langle X_L \rangle$  (brown and purple points) indicates a logical coherence time  $72.5 \pm 32.9 \mu\text{s}$ , also exceeding that of the best physical qubit,  $21.5 \mu\text{s}$ , on the device (dashed lines) (Fig. 5b). However, the fits to  $\langle X_L \rangle$  show larger error bars due to the finite fidelity of preparing the logical  $|+\rangle_L$  and  $|-\rangle_L$  states, limited by the pure dephasing of the qubits as also seen in Fig. 4d,e. Converting the measured decay times into an error per stabilizer measurement cycle, we find a logical  $X_L$  error probability of  $3.1 \pm 0.45\%$  and a logical  $Z_L$  error probability of  $2.6 \pm 1.3\%$ .

Generally, we find good agreement between the measured expectation values of the logical qubit operators and those calculated using numerical simulations, solid lines in Fig. 5a,b, accounting for finite physical qubit lifetime ( $T_1$ ) and coherence time ( $T_2$ ), residual ZZ coupling and readout errors; see Methods for details. From the numerical simulations, we extract logical decay times for  $Z_L$  and  $X_L$  operators when no errors are detected of 44.2  $\mu$ s and 59.6  $\mu$ s, which are smaller than the experimentally obtained times, but within the experimental error bars. The simulated decay times correspond to a logical  $X_L$  error probability of 4.2% and a logical  $Z_L$  error probability of 3.1% per error detection cycle. We suspect that for the  $|+\rangle_L$  state coherent errors from qubit frequency drifts during the data collection cause the deviations between data and simulations.

Finally, we discuss the probability of observing  $k$  ancilla qubits simultaneously in the  $|1\rangle$  state per error detection cycle when no errors were detected in previous cycles. We find that the probability of observing no errors slowly increases with increasing  $N$  from about 40% to 50% (Fig. 5d). From numerical simulations, we find that the probability of observing no additional errors after one cycle is between 49.9% and 50.3% per cycle, slightly larger than the experimentally observed values. We also observe experimentally that the probability of detecting more than a single ancilla qubit in the  $|1\rangle$  state per cycle is approximately suppressed exponentially. Consistent with this analysis, we find that the measured cumulative probability of not detecting an error (blue data points) decreases exponentially with increasing  $N$  (Fig. 5c). After  $N=10$  cycles, the success probability, that is the total probability that the state has remained in the code space, approaches  $10^{-4}$ , around a factor of 6 smaller than the simulated value. The difference between the simulated (dashed line) and experimentally determined success probabilities stems from the smaller simulated error probability per cycle discussed above.

### From error detection to error correction

The extended lifetime and coherence time of the logical qubit observed in our repeated quantum error detection experiment benefited critically from the fast and low-crosstalk readout of ancilla qubits, unique to our set-up. This observation indicates that neither the syndrome measurements nor the postselection extract information about the logical qubit state. The high-fidelity gates<sup>39</sup> and low-crosstalk qubit readout<sup>37</sup> we demonstrated in our experiments are directly applicable to a variety of other quantum error correction codes<sup>47–50</sup>, which also rely on repeated measurements of ancilla qubits with minimal detrimental effects on the data qubits. We therefore anticipate that quantum error correction codes realized with superconducting qubits can directly benefit from using a physical implementation inspired by the one presented here. The gate sequence we use in this work is extensible to larger surface codes, which will enable error correction<sup>40</sup> in a next key step towards using superconducting quantum devices for fault-tolerant quantum computing.

### Online content

Any methods, additional references, Nature Research reporting summaries, source data, extended data, supplementary information, acknowledgements, peer review information; details of author contributions and competing interests; and statements of data and code availability are available at <https://doi.org/10.1038/s41567-020-0920-y>.

Received: 20 December 2019; Accepted: 28 April 2020;

Published online: 08 June 2020

### References

- Zhang, J. et al. Observation of a many-body dynamical phase transition with a 53-qubit quantum simulator. *Nature* **551**, 601–604 (2017).
- Bernien, H. et al. Probing many-body dynamics on a 51-atom quantum simulator. *Nature* **551**, 579–584 (2017).
- Arute, F. et al. Quantum supremacy using a programmable superconducting processor. *Nature* **574**, 505–510 (2019).
- Preskill, J. Quantum computing in the NISQ era and beyond. *Quantum* **2**, 79 (2018).
- Cory, D. G. et al. Experimental quantum error correction. *Phys. Rev. Lett.* **81**, 2152–2155 (1998).
- Chiaverini, J. et al. Realization of quantum error correction. *Nature* **432**, 602–605 (2004).
- Schindler, P. et al. Experimental repetitive quantum error correction. *Science* **332**, 1059–1061 (2011).
- Lanyon, B. P. et al. Measurement-based quantum computation with trapped ions. *Phys. Rev. Lett.* **111**, 210501 (2013).
- Linke, N. M. et al. Fault-tolerant quantum error detection. *Sci. Adv.* **3**, e170174 (2017).
- Yao, X.-C. et al. Experimental demonstration of topological error correction. *Nature* **482**, 489–494 (2012).
- Bell, B. A. et al. Experimental demonstration of a graph state quantum error-correction code. *Nat. Commun.* **5**, 3658 (2014).
- Cramer, J. et al. Repeated quantum error correction on a continuously encoded qubit by real-time feedback. *Nat. Commun.* **7**, 11526 (2016).
- Reed, M. D. et al. Realization of three-qubit quantum error correction with superconducting circuits. *Nature* **482**, 382–385 (2012).
- Shankar, S. et al. Autonomously stabilized entanglement between two superconducting quantum bits. *Nature* **504**, 419–422 (2013).
- Ristè, D. et al. Detecting bit-flip errors in a logical qubit using stabilizer measurements. *Nat. Commun.* **6**, 6983 (2015).
- Kelly, J. et al. State preservation by repetitive error detection in a superconducting quantum circuit. *Nature* **519**, 66–69 (2015).
- Córcoles, A. D. et al. Demonstration of a quantum error detection code using a square lattice of four superconducting qubits. *Nat. Commun.* **6**, 6979 (2015).
- Ofek, N. et al. Extending the lifetime of a quantum bit with error correction in superconducting circuits. *Nature* **536**, 441–445 (2016).
- Ristè, D. et al. Deterministic entanglement of superconducting qubits by parity measurement and feedback. *Nature* **502**, 350–354 (2013).
- Negnevitsky, V. et al. Repeated multiqubit readout and feedback with a mixed-species trapped-ion register. *Nature* **563**, 527–531 (2018).
- Andersen, C. K. et al. Entanglement stabilization using ancilla-based parity detection and real-time feedback in superconducting circuits. *npj Quantum Inf.* **5**, 69 (2019).
- Bultink, C. C. et al. Protecting quantum entanglement from leakage and qubit errors via repetitive parity measurements. *Sci. Adv.* **6**, eaay3050 (2020).
- Nigg, D. et al. Quantum computations on a topologically encoded qubit. *Science* **345**, 302–305 (2014).
- Gong, M. et al. Experimental verification of five-qubit quantum error correction with superconducting qubits. Preprint at <http://arXiv.org/abs/1907.04507> (2019).
- Takita, M., Cross, A. W., Córcoles, A. D., Chow, J. M. & Gambetta, J. M. Experimental demonstration of fault-tolerant state preparation with superconducting qubits. *Phys. Rev. Lett.* **119**, 180501 (2017).
- Hu, L. et al. Quantum error correction and universal gate set operation on a binomial bosonic logical qubit. *Nat. Phys.* **15**, 503–508 (2019).
- Campagne-Ibarcq, P. et al. A stabilized logical quantum bit encoded in grid states of a superconducting cavity. Preprint at <http://arXiv.org/abs/1907.12487> (2019).
- Kitaev, A. Y. Fault-tolerant quantum computation by anyons. *Ann. Phys. (N. Y.)* **303**, 2–30 (2003).
- Dennis, E., Kitaev, A., Landahl, A. & Preskill, J. Topological quantum memory. *J. Math. Phys.* **43**, 4452–4505 (2002).
- Raussendorf, R. & Harrington, J. Fault-tolerant quantum computation with high threshold in two dimensions. *Phys. Rev. Lett.* **98**, 190504 (2007).
- Fowler, A. G., Mariantoni, M., Martinis, J. M. & Cleland, A. N. Surface codes: towards practical large-scale quantum computation. *Phys. Rev. A* **86**, 032324 (2012).
- Lidar, D. A. & Brun, T. A. *Quantum Error Correction* (Cambridge Univ. Press, 2013).
- Terhal, B. M. Quantum error correction for quantum memories. *Rev. Mod. Phys.* **87**, 307–346 (2015).
- Groen, J. P. et al. Partial-measurement backaction and nonclassical weak values in a superconducting circuit. *Phys. Rev. Lett.* **111**, 090506 (2013).
- Schmitt, V. et al. Multiplexed readout of transmon qubits with Josephson bifurcation amplifiers. *Phys. Rev. A* **90**, 062333 (2014).
- Jeffrey, E. et al. Fast accurate state measurement with superconducting qubits. *Phys. Rev. Lett.* **112**, 190504 (2014).
- Heinsoo, J. et al. Rapid high-fidelity multiplexed readout of superconducting qubits. *Phys. Rev. Appl.* **10**, 034040 (2018).
- Barends, R. et al. Superconducting quantum circuits at the surface code threshold for fault tolerance. *Nature* **508**, 500–503 (2014).

39. Rol, M. A. et al. Fast, high-fidelity conditional-phase gate exploiting leakage interference in weakly anharmonic superconducting qubits. *Phys. Rev. Lett.* **123**, 120502 (2019).
40. Versluis, R. et al. Scalable quantum circuit and control for a superconducting surface code. *Phys. Rev. Appl.* **8**, 034021 (2017).
41. Johnson, J. E. et al. Heralded state preparation in a superconducting qubit. *Phys. Rev. Lett.* **109**, 050506 (2012).
42. Ristè, D., van Leeuwen, J. G., Ku, H.-S., Lehnert, K. W. & DiCarlo, L. Initialization by measurement of a superconducting quantum bit circuit. *Phys. Rev. Lett.* **109**, 050507 (2012).
43. Koch, J. et al. Charge-insensitive qubit design derived from the Cooper pair box. *Phys. Rev. A* **76**, 042319 (2007).
44. Reed, M. D. et al. Fast reset and suppressing spontaneous emission of a superconducting qubit. *Appl. Phys. Lett.* **96**, 203110 (2010).
45. Krinner, S. et al. Engineering cryogenic setups for 100-qubit scale superconducting circuit systems. *Eur. Phys. J. Quantum Technol.* **6**, 2 (2019).
46. Takita, M. et al. Demonstration of weight-four parity measurements in the surface code architecture. *Phys. Rev. Lett.* **117**, 210505 (2016).
47. Bacon, D. Operator quantum error-correcting subsystems for self-correcting quantum memories. *Phys. Rev. A* **73**, 012340 (2006).
48. Bombin, H. & Martin-Delgado, M. A. Topological quantum distillation. *Phys. Rev. Lett.* **97**, 180501 (2006).
49. Chamberland, C., Zhu, G., Yoder, T. J., Hertzberg, J. B. & Cross, A. W. Topological and subsystem codes on low-degree graphs with flag qubits. *Phys. Rev. X* **10**, 011022 (2020).
50. Li, M., Miller, D., Newman, M., Wu, Y. & Brown, K. R. 2D compass codes. *Phys. Rev. X* **9**, 021041 (2019).

**Publisher's note** Springer Nature remains neutral with regard to jurisdictional claims in published maps and institutional affiliations.

© The Author(s), under exclusive licence to Springer Nature Limited 2020

## Methods

**Device fabrication.** The device in Fig. 2 consists of seven qubits coupled to each other in the geometry shown in Fig. 1a. The resonator, coupling and qubit structures are defined using photolithography and reactive ion etching from a 150-nm thin niobium film sputtered onto a high-resistivity intrinsic silicon substrate. To establish a well connected ground plane, we add airbridges to the device. Airbridges are also used to cross signal lines, that is, for the flux and charge lines to cross the feedlines. The aluminium-based Josephson junctions of the qubits are fabricated using electron-beam lithography.

**Experimental set-up.** The seven-qubit device is installed at the base plate of a cryogenics set-up<sup>45</sup> (Extended Data Fig. 1). Here, the qubits (indicated by their labels) are controlled by flux and control arbitrary waveform generators (AWGs) through a series of microwave cables each with attenuators and filters, such as bandpass filters (BP), lowpass filters (LP), highpass filters (HP) and Eccosorb filters, installed as indicated. The flux pulses and microwave drive pulses are generated using AWGs with eight channels and a sampling rate of 2.4 GSa s<sup>-1</sup>. The flux pulses are combined with a d.c. current using a bias tee. The baseband microwave control pulses are generated at an intermediate frequency (IF) of 100 MHz and then upconverted to microwave frequencies using in-phase–quadrature (IQ) mixers installed on upconversion boards (UC). The multiplexed readout pulses, see also Supplementary Information, are generated and detected using a control system based on a field-programmable gate array (FPGA; Zurich Instruments UHFQA) with a sampling rate of 1.8 GSa s<sup>-1</sup>. The measurement signals at the outputs of the sample are amplified using a wide-bandwidth near-quantum-limited travelling wave parametric amplifier (TWPA)<sup>51</sup> connected to isolators at its input and output. Moreover, we installed bandpass filters in the output lines to suppress amplifier noise outside the bandwidth of interest. The output signals are further amplified by high-electron-mobility transistor (HEMT) amplifiers and additional amplifiers at room temperature (WAMP). After amplification, the signals are downconverted (DC) and processed using the weighted integration units of the UHFQAs.

**Numerical simulations.** We model the dynamics of our seven-qubit quantum system with a master equation given by

$$\dot{\rho} = -\frac{i}{\hbar}[H(t), \rho] + \sum_i \left[ \hat{c}_i \rho \hat{c}_i^\dagger - \frac{1}{2} \left( \hat{c}_i^\dagger \hat{c}_i \rho + \rho \hat{c}_i^\dagger \hat{c}_i \right) \right] \quad (6)$$

where  $\rho$  is the density matrix describing the system at time  $t$  and  $H(t)$  is the Hamiltonian, the time dependence of which models the applied gate sequence. The collapse operators  $\hat{c}_i$  model incoherent processes. We solve the master equation numerically<sup>52</sup>. To simplify the description of the system's time evolution, we consider the Hamiltonian to be piecewise constant; see details in ref.<sup>21</sup>. In addition, we include the Hamiltonian

$$H_{ZZ}/\hbar = \sum_{ij} \alpha_{ij} |1\rangle_{ij}\langle 1|$$

modelling the residual ZZ coupling  $\alpha_{ZZ}$  shown in Supplementary Information. The incoherent errors are described by the Lindblad terms in equation (6) with

$$\begin{aligned} \hat{c}_{T_{1,i}} &= \sqrt{\frac{1}{T_{1,i}}} \sigma_{-,i} \\ \hat{c}_{T_{2,i}} &= \sqrt{\frac{1}{2} \left( \frac{1}{T_{2,i}} - \frac{1}{2T_{1,i}} \right)} \sigma_{z,i} \end{aligned}$$

where  $T_{1,i}$  and  $T_{2,i}$  are the lifetime and decoherence time (Ramsey decay time) of qubit  $i$ .

To simulate the ancilla measurement, we consider the operators for a positive-operator valued measure (POVM):

$$M_0 = \sqrt{P(0|0)} |0\rangle\langle 0|_A + \sqrt{P(0|1)} |1\rangle\langle 1|_A \quad (7)$$

$$M_1 = \sqrt{P(1|0)} |0\rangle\langle 0|_A + \sqrt{P(1|1)} |1\rangle\langle 1|_A \quad (8)$$

for the outcomes 0 and 1 respectively, where  $P(i|j)$  are the experimentally determined probabilities of measuring state  $i$  when preparing state  $j$ . We choose for simplicity the POVM operators corresponding to minimal disturbance measurements<sup>53</sup>, as these POVM operators will mostly remove coherences similar to the real physical measurements. We evaluate the probability for each ancilla measurement outcome using  $p_i = \text{Tr}(M_i \rho M_i^\dagger)$  for  $i \in \{0, 1\}$ . The resulting density matrix given a certain measurement outcome  $i$  is calculated as  $\rho \rightarrow M_i \rho M_i^\dagger / p_i$ .

## Data availability

The authors declare that the data supporting the findings of this work are available online at the ETH Zurich repository for research data <https://doi.org/10.3929/ethz-b-000410090>.

## Code availability

The codes used for experimental control are available from the corresponding author on reasonable request.

## References

51. Macklin, C. et al. A near-quantum-limited Josephson traveling-wave parametric amplifier. *Science* **350**, 307–310 (2015).
52. Johansson, J. R., Nation, P. D. & Nori, F. QuTiP 2: a Python framework for the dynamics of open quantum systems. *Comput. Phys. Commun.* **184**, 1234–1240 (2013).
53. Wiseman, H. & Milburn, G. *Quantum Measurement and Control* (Cambridge Univ. Press, 2010).

## Acknowledgements

We are grateful for feedback from K. Brown and A. Darmawan. We acknowledge contributions to the measurement set-up from S. Storz, F. Swiadek and T. Zellweger. We acknowledge financial support by the Office of the Director of National Intelligence (ODNI), Intelligence Advanced Research Projects Activity (IARPA), via the US Army Research Office grant W911NF-16-1-0071, by the National Centre of Competence in Research Quantum Science and Technology (NCCR QSIT), a research instrument of the Swiss National Science Foundation (SNSF), by the EU Flagship on Quantum Technology H2020-FETFLAG-2018-03 project 820363 OpenSuperQ, by the SNFS R'Equip grant 206021-170731 and by ETH Zurich. The views and conclusions contained herein are those of the authors and should not be interpreted as necessarily representing the official policies or endorsements, either expressed or implied, of the ODNI, IARPA or the US Government.

## Author contributions

C.K.A. designed the device and A.R., S.K., G.J.N. and M.G. fabricated the device. C.K.A., A.R., S.L. and N.L. developed the experimental control software. C.K.A., A.R., S.K. and N.L. installed the experimental set-up. C.K.A., A.R. and S.L. characterized and calibrated the device and the experimental set-up. C.K.A. carried out the main experiment and analysed the data. C.K.A. performed the numerical simulations. C.E. and A.W. supervised the work. C.K.A., A.R. and S.L. prepared the figures for the manuscript. C.K.A. wrote the manuscript with input from all coauthors.

## Competing interests

The authors declare no competing interests.

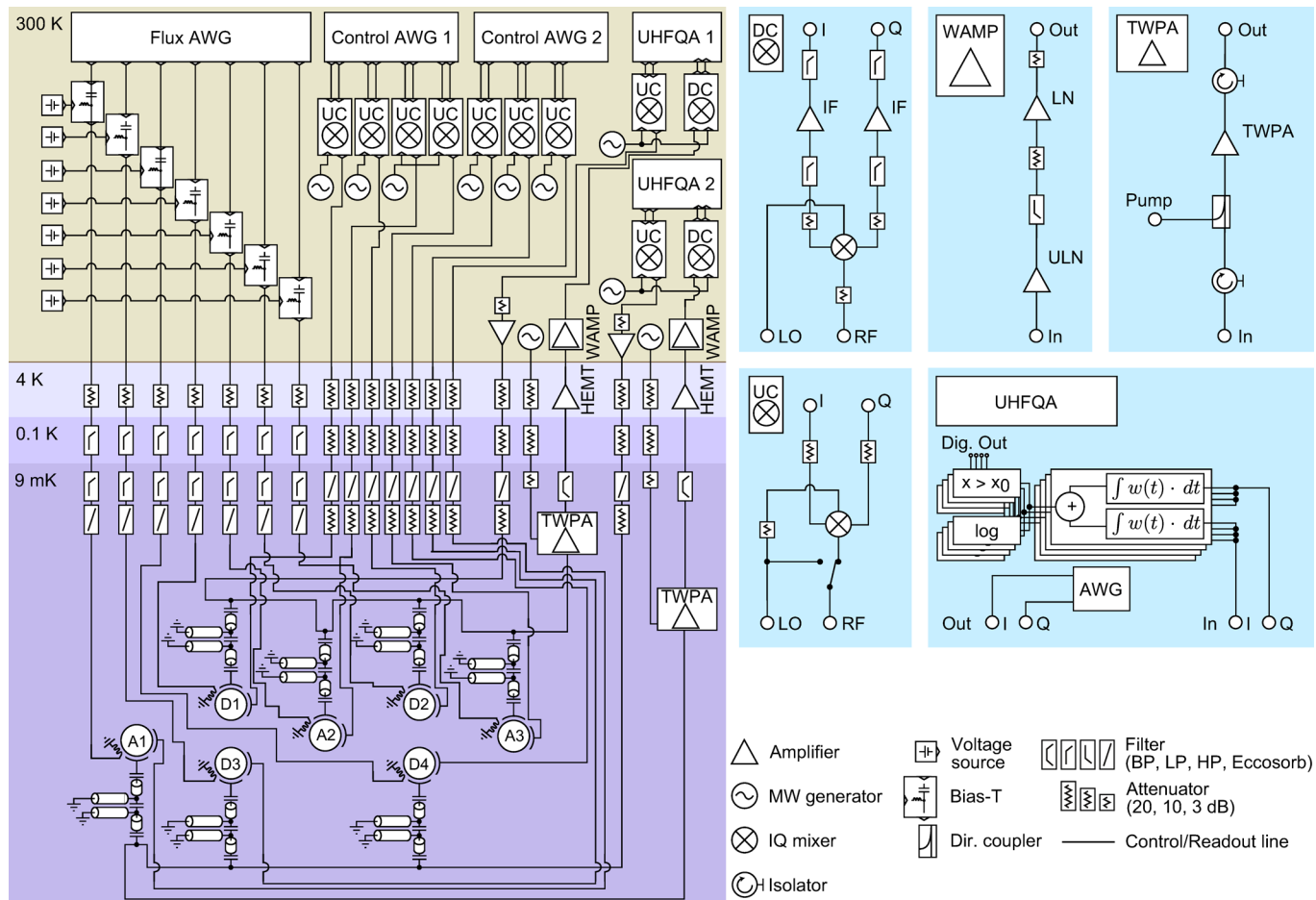
## Additional information

**Extended data** is available for this paper at <https://doi.org/10.1038/s41567-020-0920-y>.

**Supplementary information** is available for this paper at <https://doi.org/10.1038/s41567-020-0920-y>.

**Correspondence and requests for materials** should be addressed to C.K.A.

**Reprints and permissions information** is available at [www.nature.com/reprints](http://www.nature.com/reprints).



**Extended Data Fig. 1 | Experimental setup.** Experimental setup described in Methods.